The Lyman-alpha Solar Telescope (LST) for the ASO-S mission – II. design of LST

Bo Chen[1,2], Hui Li[3,4], Ke-Fei Song[1], Quan-Feng Guo[1], Pei-Jie Zhang[1], Ling-Ping He[1,2], Shuang Dai[1],
Xiao-Dong Wang[1], Hai-Feng Wang[1], Chun-Long Liu[1], Hong-Ji Zhang[1], Guang Zhang[1], Yunqi Wang[1],
Shi-Jie Liu[1,2], Hong-Xin Zhang[1], Lei Liu[1], Shi-Lei Mao[1], Yang Liu[1], Jia-Hao Peng[1], Peng Wang[1],
Liang Sun[1], Yang Liu[1], Zhen-Wei Han[1], Yan-Long Wang[1], Kun Wu[1], Guang-Xing Ding[1], Peng Zhou[1],
Xin Zheng[1], Ming-Yi Xia[1], Qing-Wen Wu[1], Jin-Jiang Xie[1], Ya Chen[1], Shu-Mei Song[1], Hong Wang[5],
Bo Zhu[5], Chang-Bo Chu[5], Wen-Gang Yang[5], Li Feng[3,4], Yu Huang[3,4], Wei-Qun Gan[3,4], Ying Li[3,4],
Jing-Wei Li[3,4], Lei Lu[3,4], Jian-Chao Xue[3,4], Bei-Li Ying[3,4], Ming-Zhe Sun[6], Cheng Zhu[7], Wei-Min Bao[7],
Lei Deng[7] and Zeng-Shan Yin[7]

[1] Changchun Institute of Optics, Fine Mechanics and Physics, Chinese Academy of Sciences, Changchun 130033, China
[2] State Key Laboratory of Applied Optics, Changchun 130033, China
[3] Key Laboratory of Dark Matter and Space Astronomy, Purple Mountain Observatory, Chinese Academy of Sciences, Nanjing 210034, China; *nj.lihui@pmo.ac.cn*
[4] School of Astronomy and Space Science, University of Science and Technology of China, Hefei 230026, China
[5] Xi'an Institute of Optics and Precision Mechanics, Chinese Academy of Sciences, Xi'an 710119, China
[6] Shandong University, Weihai 264209, China
[7] Innovation Academy for Microsatellites, Chinese Academy of Sciences, Shanghai 201210, China

Abstract As one of the three payloads for the Advanced Space-based Solar Observatory (ASO-S) mission, the Lyman-alpha (Lyα) Solar Telescope (LST) is composed of three instruments: a Solar Corona Imager (SCI), a Lyα Solar Disk Imager (SDI) and a full-disk White-light Solar Telescope (WST). When working in-orbit, LST will simultaneously perform high-resolution imaging observations of all regions from the solar disk to the inner corona up to $2.5\,R_\odot$ ($R_\odot$ stands for the mean solar radius) with a spatial resolution of $4.8''$ and $1.2''$ for coronal and disk observations, respectively, and a temporal resolution of $30-120\,\mathrm{s}$ and $1-120\,\mathrm{s}$ for coronal and disk observations, respectively. The maximum exposure time can be up to $20\,\mathrm{s}$ due to precise pointing and image stabilization function. Among the three telescopes of LST, SCI is a dual-waveband coronagraph simultaneously and independently observing the inner corona in the HI Lyα ($121.6\pm10\,\mathrm{nm}$) line and white light (WL) ($700\pm40\,\mathrm{nm}$) wavebands by using a narrowband Lyα beam splitter and has a field of view (FOV) from 1.1 to $2.5\,R_\odot$. The stray-light suppression level can attain $<10^{-6}\,B_\odot$ ($B_\odot$ is the mean brightness of the solar disk) at $1.1\,R_\odot$ and $\leq5\times10^{-8}\,B_\odot$ at $2.5\,R_\odot$. SDI and WST are solar disk imagers working in the Lyα line and $360.0\,\mathrm{nm}$ wavebands, respectively, which adopt an off-axis two-mirror reflective structure with an FOV up to $1.2\,R_\odot$, covering the inner coronal edge area and relating to coronal imaging. We present the up-to-date design for the LST payload.

Key words: telescopes — instrumentation: high angular resolution — Sun: flares — Sun: coronal mass ejections (CMEs) — Sun: UV radiation

1 INTRODUCTION

The Advanced Space-based Solar Observatory (ASO-S) is the first solar mission dedicated to solar physics in China. As one of the three payloads, the Lyman-alpha (Lyα) Solar

Telescope (LST) is composed of three instruments: a dual-waveband Solar Corona Imager (SCI), a Lyα Solar Disk Imager (SDI) and a White-light Solar Telescope (WST). LST is mounted on top of the ASO-S satellite platform facing the Sun. The satellite platform guarantees a $36''$ point-

ing accuracy to the Sun with a pointing stability of 1.8″ per second. The SCI and SDI have image stabilization functions by using the guide telescope (GT) and active mirrors. The GT and image stabilization device can achieve 10″ pointing accuracy. The installation position of LST on the platform is diagramed in Figure 1.

When LST is in-orbit, three instruments and four channels work simultaneously. LST will observe all areas from the solar disk to the inner corona up to $2.5\,R_\odot$ in the Lyα line, and the coronal polarization images in 700.0 nm waveband, along with the solar disk image in 360.0 nm waveband. The scientific objectives are summarized below, and please refer to Gan et al. (2019), Li et al. (2019) and Feng et al. (2019a) for details.

1) What is the relationship among solar fares, coronal mass ejections (CME) and eruptive prominences?

2) What triggers flares and CMEs, and how do their parameters evolve during the eruptive process?

3) What are the acceleration mechanisms of CMEs in the inner corona? What are their kinetic behaviors?

4) How are shock waves formed and solar energetic particles accelerated by shock waves?

5) What are the physical properties and processes of white light (WL) flares?

6) What are the physical properties of CME source regions?

In order to address these questions, we have been developing the LST for solar observations from the disk to $2.5\,R_\odot$ in the Lyα line, and 700.0 nm and 360.0 nm wavebands. The LST specifications are listed in Table 1.

The scientific objectives and overview have been presented in Li et al. (2019) (Paper I) and the data products and diagnostics have been presented in Feng et al. (2019a) (Paper III). In this paper (Paper II), we describe the detailed design of the LST instruments in Section 2, including optical design, stray-light suppression, mechanical structure, thermal control and electronics. We present the test and calibration of LST in Section 3 and summarize the paper in Section 4.

2 DESCRIPTION OF INSTRUMENTS

In the past decades, a number of solar missions have been conducted and have provided high-quality imaging and spectroscopic data, such as the Extreme-ultraviolet Imaging Telescope (EIT) and the Large Angle Spectroscopic Coronagraph (LASCO) onboard the Solar and Heliospheric Observatory (SOHO) mission, the Atmospheric Imaging Assembly (AIA) onboard the Solar Dynamics Observatory (SDO) satellite, and the Multi Element Telescope for Imaging and Spectroscopy (METIS) coronagraph onboard the Solar Obiter satellite. LASCO includes three coronagraphs: C1, C2 and C3. The

C1 coronagraph is an internally-occulted coronagraph and images the inner corona from 1.1 to $3\,R_\odot$ with spatial resolution of 11.2″, while the C2 and C3 coronagraphs are externally occulted. The C2 coronagraph overlaps the outer field of view (FOV) of the C1 coronagraph and images the corona from 1.5 to $6\,R_\odot$ with spatial resolution of 22.8″, and the C3 coronagraph images the outer corona from 3.7 to $30\,R_\odot$ with spatial resolution of 112″(Brueckner et al. 1995). METIS is the first coronagraph in Lyα wavelength, which has the capability of imaging the corona in the Lyα line with an FOV from 1.5° to 2.9°, corresponding to 1.5 to $3\,R_\odot$ at minimum perihelion (0.28 AU) and has a spatial resolution of 20″. METIS will be in space along with the Solar Orbiter mission in 2020 (Fineschi et al. 2012; Landini et al. 2017; Antonucci et al. 2019).

Since the 1980s, key technologies have been studied at the Changchun Institute of Optics, Fine Mechanics and Physics (CIOMP), which include super polishing of mirrors, far ultraviolet (FUV) and extreme ultraviolet (EUV) multilayer film (Li et al. 2014), high sensitivity FUV and EUV detectors, and FUV and EUV calibration. Based on these key technologies, some FUV and EUV instruments have been developed in CIOMP, such as the Chang'E-3 EUV camera (Chen et al. 2014) and FY-3D Wide Field Aurora Imager (WAI) (Zhang et al. 2019), which were launched in 2013 and 2017, respectively. The Chang'E-3 EUV camera was developed for watching Earth plasma in the 30.4 nm waveband, which has a sensitivity of $0.05\,\mathrm{counts\,s^{-1}\,R^{-1}\,pixel^{-1}}$, an FOV of 15° and a spatial resolution of 0.8° (Chen & He 2011). Currently, WAI is operating in orbit for monitoring the distribution and changes in aurorae. This instrument has a wavelength region from 140 nm to 180 nm, an FOV of 130°×130°, a spatial resolution of 0.8° and a sensitivity of $0.05\,\mathrm{counts\,s^{-1}\,R^{-1}\,pixel^{-1}}$. Now the FY-3 solar X-EUV imager is being developed at CIOMP, which has an FOV of 42′, a spatial resolution of 5″ in the 19.5 nm waveband and 10″ in X-ray. The solar X-EUV imager has a common axis for X-ray grazing optics and EUV multilayer film implemented in normal optics, and has a common CCD detector. The solar X EUV imager will be launched at the end of next year.

The Lyα coronagraph has been investigated for around 10 years, and a number of key technologies have been studied. Since 2018, the ASO-S satellite project started to be implemented. LST is composed of an SCI and two full-disk imagers, named SDI and WST, respectively. Imaging the solar corona in the Lyα and WL simultaneously is the advantage of SCI (Wang et al. 2018). In order to separate the coronal radiation of 121.6 nm and 700.0 nm, a narrow-band Lyα beam splitter is used in front of the focal plane, and the transmitted and reflected beams feed the Lyα and
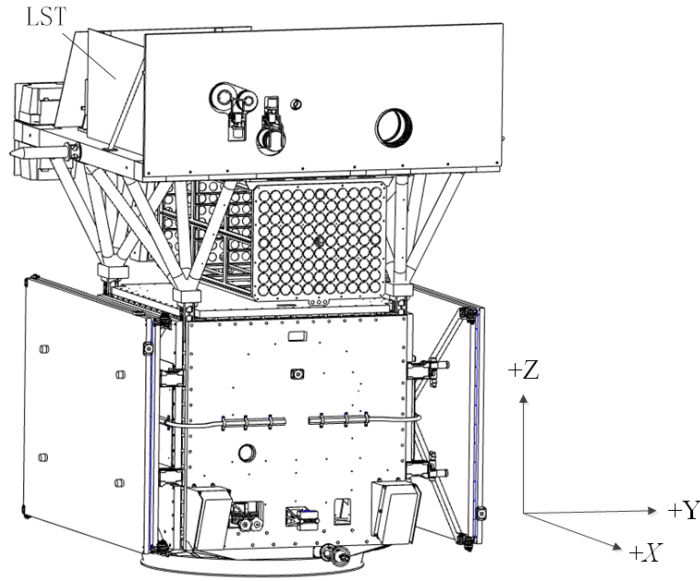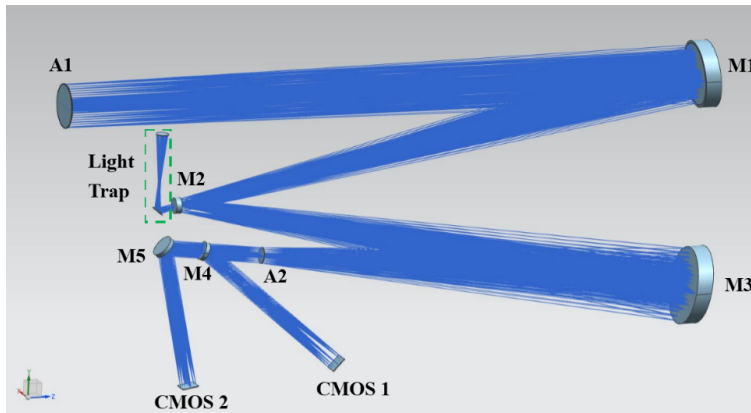
Fig. 1 LST mounting position and coordinate system.

Fig. 2 Schematic optical layout of SCI.

Table 1 LST Specifications

Parameter	SCI_UV	SCI_WL	SDI	WST
Aperture (mm)	60	60	60	130
Wavelength (nm)	121.6±10.0	700±40	121.6±7.5	360.0±2.0
FOV ($R_\odot$)	1.1 – 2.5	1.1 – 2.5	1.2	1.2
Spatial resolution ($''$)	4.8	4.8	1.2	1.2
Detector pixel size (μm)	11	11	10	10
Cadence (s) [1]	15 – 30	30 – 60[2]	4 – 40	1 – 120
pB polarizer angle (°)		0, ±60		

[1] Nominal cadence. Other cadences are available on demand within the instrument limit; [2] Cadence for a set of pB images, i.e., three images with the angle of the linear polarizer at 0° and ±60°.

and WL channels of SCI, respectively. Another narrow-band filter is positioned in front of the Lyα detector to suppress the out-of-band radiation, and only for 121.6 nm coronal imaging. In addition, a 700.0 nm narrowband filter and a polarizer are arranged in front of the WL detector. The filter can suppress out-of-band radiation to achieve high-resolution coronal imaging at 700.0 nm, while the polarizer can switch quickly to perform coronal imaging in three different polarization angles (Feng et al. 2019b).

Both SDI and WST adopt an off-axis two-mirror reflective optical layout, working in the Lyα line (121.6±7.5 nm) and 360±2 nm, respectively. A Lyα filter

Table 2 SCI Optical Parameters

Effective focal length	972 mm
Primary mirror	Off-axis parabolic
Second mirror, inner occulter	Convex spherical
Third mirror	Off-axis ellipsoidal
Lyot stop	Circular aperture
Beam splitter	Flat
Fifth (folding) mirror	Flat
Lyα detector	121.6 nm
WL detector	700.0 nm
Detector pixel size	11 μm
Spatial resolution	4.6$''$

is used at the entrance of SDI to prevent strong solar radiation from entering the optical system, which may result in a high internal temperature level and excessive temperature gradient. Meanwhile, SDI relies on a Lyα narrowband multilayer film mirror that only reflects radiation in the 121.6 nm band, thus avoiding the out-of-band solar radiation reaching the focal plane assembly. In the front of the detector, a Lyα filter is still affixed to further reduce out-of-band solar radiation.

Similarly, for WST a 360 nm filter is installed at the entrance to prevent visible radiation from the Sun and the influence of space particles from entering the WST optical system. In addition, a 360 nm narrowband filter is used to filter the out-of-band radiation that may affect the imaging quality in front of the detector.

2.1 Optical Design

Firstly, according to the requirements of LST technical specifications, the parameters are calculated, which include the orbital altitude and characteristics, reflectance of optical components, transmittance of filters and quantum efficiency of detectors, geometrical area of the entrance pupil and focal lengths of SCI, SDI and WST. Subsequently, analysis of LST is performed to simulate the imaging quality of LST.

2.1.1 Solar coronal imager

SCI will operate at an orbital attitude of 720 km and will take high spatial resolution images of the corona in both the Lyα line and 700.0 nm waveband simultaneously. Considering the observed brightness of the corona, along with the angular resolution and temporal resolution requirements, geometrical area of the entrance pupil is related to the pixel solid angle, transmittance of the optical system, quantum efficiency and electron counts of the detector, which can be calculated as follows

$$Ne = A \times \omega \times \tau \times \epsilon \times B_\odot, \quad (1)$$

where Ne is electron counts per pixel, A is geometrical area of the entrance for SCI, ω is the solid angle corresponding to a single pixel, τ is transmittance of the SCI optical system, ϵ is quantum efficiency of the detector and $B_\odot$ is brightness of the Sun.

Based on the signal-to-noise ratio (SNR) requirement, the geometrical areas of the entrance pupil for both the Lyα and 700.0 nm channels are determined. The area is not less than 27.4 cm^2 for the Lyα channel when the coronal brightness is not less than 5.34×10^{10} ph cm^{-2} s^{-1} ster^{-1}. The entrance pupil geometrical area for the 700.0 nm channel should be not less than 24.0 cm^2 when the relative brightness of the target is not less than 1.70×10^{-9} B$_\odot$. For comprehensive consideration, 28.0 cm^2 of the entrance pupil area is utilized. Finally, the focal length of LST is at least 945 mm according to the pixel size, angular resolution and FOV requirements.

SCI is a Lyot-type dual-waveband internally occulted reflecting and off-axis coronagraph. The SCI optical layout is illustrated in Figure 2, and the optical parameters are listed in Table 2. The entrance aperture (A1) allows the solar disk and corona to illuminate the super polished, off-axis parabolic primary mirror (M1). M1 forms an image of the solar disk and the corona on a convex secondary mirror (M2), which is the first focal plane with a cone-shaped hole, working as the internal occulter to reject solar light, which is absorbed by the light trap located behind M2. Then the coronal light remains and is reflected from M2 to an off-axis ellipsoidal third mirror (M3). A beam splitter (M4) composed of multilayer film is used to only reflect the Lyα emission from the corona to the Lyα detector (CMOS 1) and the WL emission from the corona is transmitted and imaged on the WL detector (CMOS 2). A Lyot stop (A2) is placed in the conjugate plane of A1 imaged by M1, M2 and M3, to block the light diffracted from the edge of A1. The polarimeter assembly is arranged between the fifth mirror M5 and CMOS 2, but is not shown in Figure 2. The aperture of M1 is sufficiently larger than the solar beam, and consequently A1 is the only source of diffracted light. The conicity of the cone-shaped hole matches the F-number and off-axis angle of M1 to avoid scattering caused by light illuminating the inside wall of the hole.

The optical design of SCI is optimized by geometrical ray tracing calculations with Zemax OpticStudio. The imaging performance of the design can be evaluated by using the spot diagram in Figure 3, the modulation transfer function (MTF) in Figure 4 and the encircled energy curves in Figure 5. The root mean square (RMS) spot radius for both cases is small, down to the max of 10 μm at 700.0 nm and 121.6 nm. MTF at the Nyquist frequency of 50 lp mm^{-1} is better than 0.4 and 0.3 at 121.6 nm and 700.0 nm, respectively. The encircled energy distribution
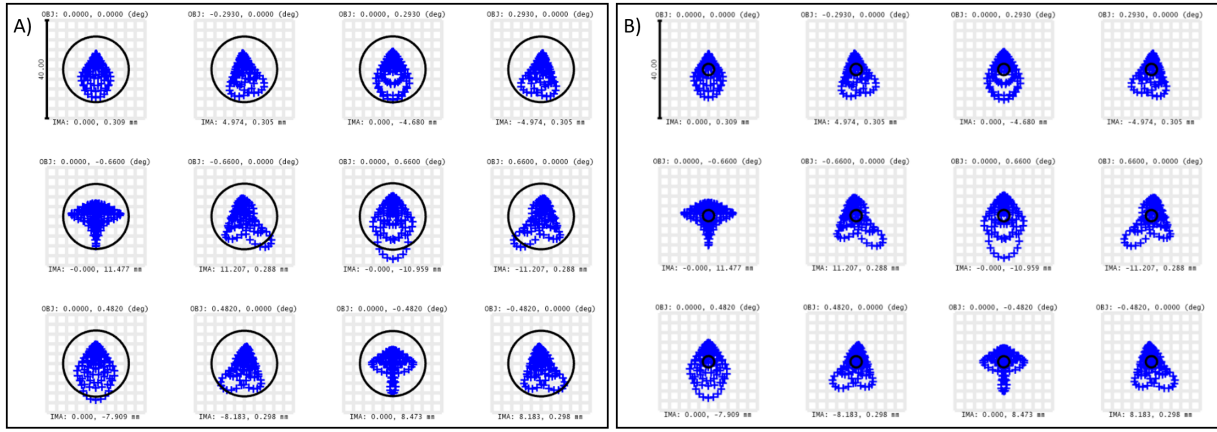
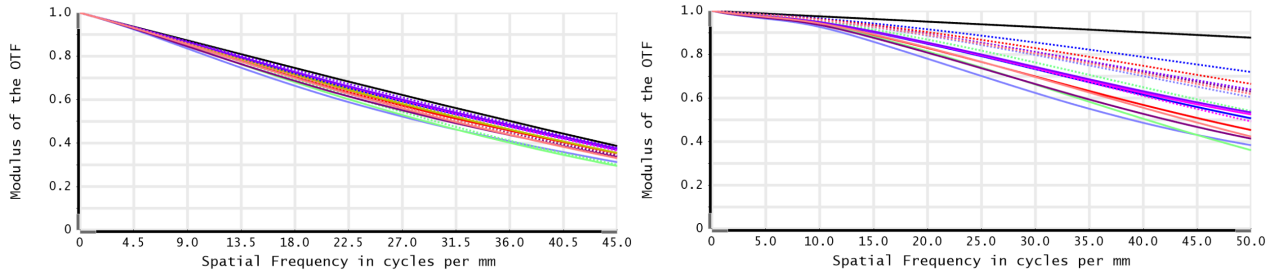**Fig. 3** Spot diagram of SCI at 700.0 nm (*left*) and 121.6 nm (*right*).

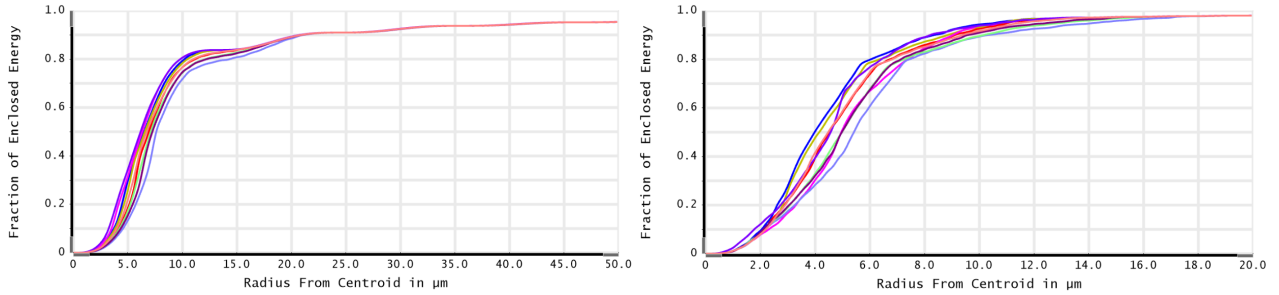**Fig. 4** MTF curves for SCI at 700.0 nm (*left*) and 121.6 nm (*right*).

Fig. 5 Encircled energy distribution curves for SCI at 700.0 nm (*left*) and 121.6 nm (*right*).

curves demonstrate how energy in the SCI optical system is concentrated.

An FUV multilayer film mirror of La/MgF$_2$ material is employed as the beam splitter (M4) (Wang et al. 2018), which only reflects Lyα radiation. The reflectance is greater than 40% with a bandwidth of 5 nm, while the transmittance at 700.0 nm is greater than 70%. The reflectance distributions of all the mirrors are plotted in Figure 6 (left). SCI has an optical system transmittance of 0.07 at 700.0 nm and a system transmittance of 0.1 at 121.6 nm, as depicted in Figure 7, which satisfies the SCI energy requirement. The spectral resolutions are less than 7.5 nm at 121.6 nm and less than 2.5 nm at 700.0 nm from the simulation results shown in Figure 7.

2.1.2 Stray-light suppression of SCI

Since the brightness of the corona is extremely weak compared to that of the solar disk, stray-light suppression becomes the most important issue in the design of the SCI coronagraph. Three main stray-light sources need to be suppressed. The first is direct light from the solar disk, then scattered light from the primary mirror (M1) and finally diffracted light from the edge of the entrance aperture (A1).

In order to eliminate direct light from the solar disk, the secondary mirror (M2) with a cone-shaped hole is designed at the focal position of M1 to ensure the direct solar light within the FOV up to 1.1 R$_\odot$ passes through the hole and enters the rear light trap. For the diffracted light from the edge of entrance aperture (A1), the Lyot stop (A2) is
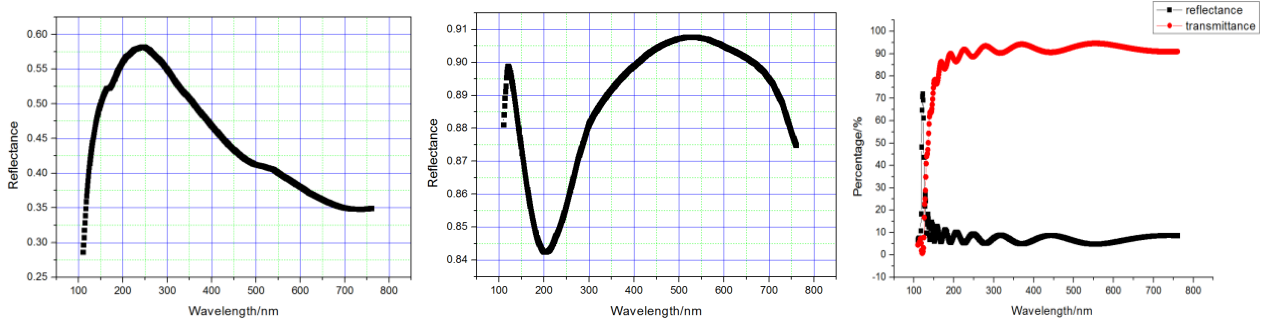
Fig. 6 *Left*: Reflectance curves for the primary mirror (M1) of SCI. *Middle*: The same reflectance curves for the secondary mirror (M2), third mirror (M3) and fifth mirror (M5). *Right*: Reflectance (*black*) and transmittance (*red*) curves for beam splitter (M4).
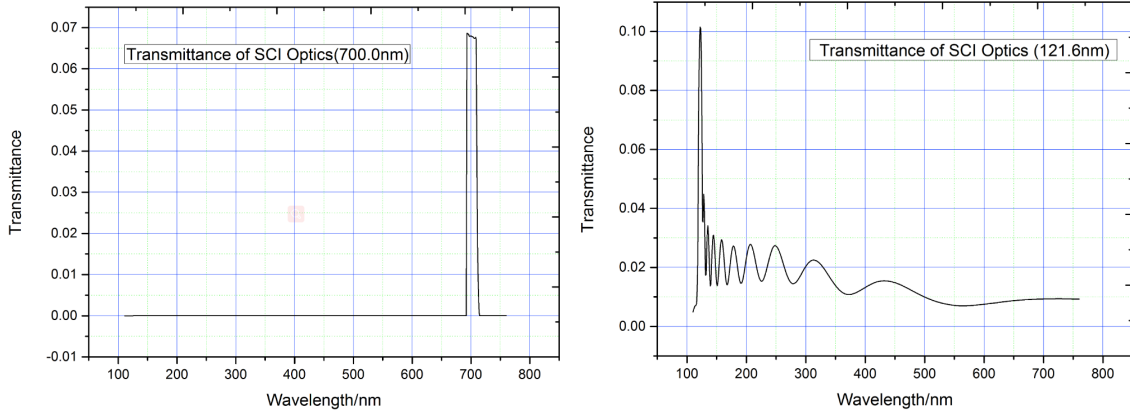

Fig. 7 Transmittance distribution of SCI for 700.0 nm (*left*) and 121.6 nm (*right*) wavebands.

placed in the conjugate plane of A1 imaged by M1, M2 and M3, to block the diffracted light. The diffracted stray-light is simulated with TracePro software as displayed in Figure 8. The inner diameter of the Lyot stop is preferably 96% of the theoretical size of the light, so that it can completely block the diffracted stray-light without losing image quality.

Since the solar light directly illuminates the surface of the primary mirror (M1), strongly scattered light is generated, which contributes the majority of the stray-light in SCI. The scattered stray-light is mainly related to the surface roughness. To calculate the contribution of surface roughness to stray-light, the Harvey-Shack ABg Bidirectional Reflectance Distribution Function (BRDF) model is applied to characterize the surface roughness of the primary mirror. This model is suitable for the scattering of optical super-polished surfaces mainly caused by surface roughness and the surface roughness is relatively low with respect to the wavelength. The scattering of SCI mirrors is completely suitable for this model. The distribution function of a surface with a roughness σ is expressed

in Equation (2) (Sandri et al. 2018).

$$\begin{aligned}
\mathrm{BRDF}(\theta) &= \frac{A}{B + (\sin\theta)^g} \\
&= \frac{\triangle n^2}{8\pi}\left[\frac{(\frac{2\pi}{\lambda})^4\sigma^2 L^2}{1 + (\frac{2\pi}{\lambda}L\sin\theta)^2}\right]
\end{aligned} \tag{2}$$

with

$$A = \frac{\triangle n^2\sigma^2\pi}{2\lambda^2}, B = \left(\frac{\lambda}{2\pi L}\right)^2, g = 2 \tag{3}$$

where $\triangle n$ is the change in refractive index ($\triangle n = 2$ for mirrors), λ is the wavelength and L is the auto-correlation length. The auto-correlation length (L) is generally evaluated with the breakpoints of the Harvey-Shack BRDF model, which is related to scattering characteristics of the surface. We refer readers to Sandri et al. (2018) for more details about definition and description about it. In our simulation, L is taken to be 10 µm.

Simulation analysis of scattered stray-light is performed with Trace Pro software. Figure 9 presents the simulation results of SCI stray-light for the 700.0 nm channel and Lyα line channel. To fulfill the requirement, the roughness RMS value of the primary mirror of SCI should be lower than 0.3 nm.
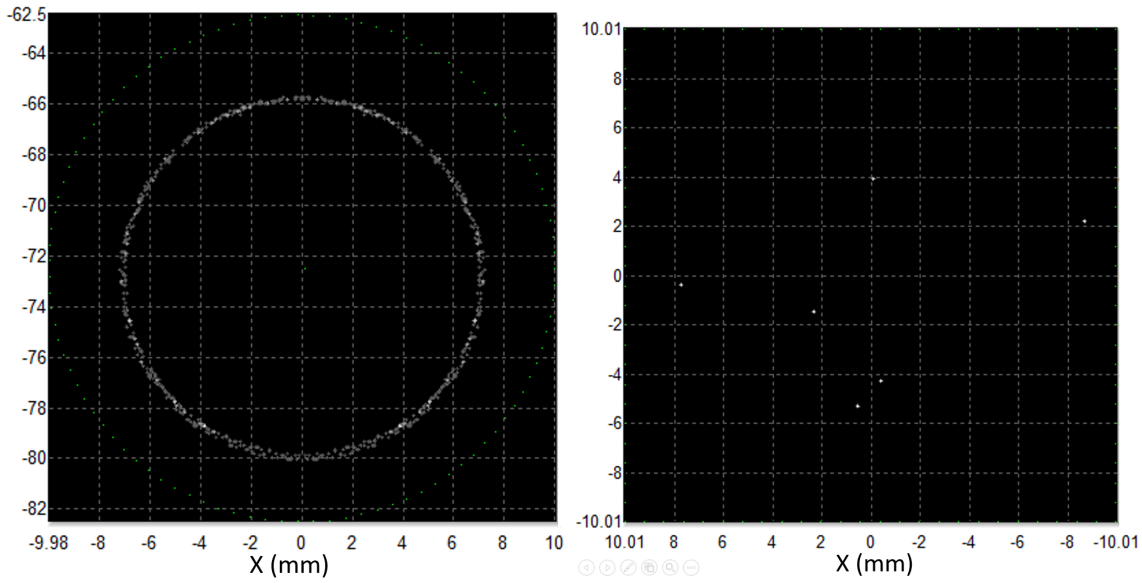
Fig. 8 *Left*: Distribution of diffracted light on the Lyot stop position. *Right*: Distribution of diffracted light on the SCI imaging position.

2.1.3 Solar Disk Imager and White-Light Solar Telescope

Both SDI and WST adopt an off-axis two-mirror reflective optical layout, which focuses the solar disk on the detectors with an FOV up to 38′ and a spatial-resolution of 1.2″, and work in the Lyα line and 360 nm waveband, respectively. The off-axis two-mirror reflective optical layout of SDI is used to reduce the number of optical components without affecting the imaging quality. A Lyα band-pass filter is arranged at the entrance of SDI to reflect the visible and infrared radiation and prevent strong solar radiation from entering the optical system. Otherwise, it may result in high internal temperature and excessive temperature gradient inside the SDI. In addition, a primary mirror with narrowband multilayer film is applied and a Lyα narrowband filter is arranged in front of the focal plane assembly to further reduce out-of-band radiation. Similarly, a 360 nm bandpass filter is positioned at the entrance of WST to reflect the visible and infrared radiation and prevent solar radiation from entering the optical system. In order to achieve high spectral purity, a 360 nm narrowband filter is also located in the front of the focal plane assembly to suppress out-of-band solar radiation. SDI and WST have optical system transmittances of 0.106 at 121.6 nm and 0.056 at 360 nm, respectively, as plotted in Figure 13, which satisfies the energy requirements.

Based on the SNR and radiation energy requirements, the geometrical area of the entrance pupil for SDI and WST should be no less than $13.3\,\mathrm{cm}^2$. The focal length of SDI and WST should be no less than 3600 mm according to the pixel size, angular resolution and FOV requirements. The optical parameters are listed in Table 3.

Table 3 SDI and WST Optical Parameters

Instrument	Item	Design
SDI	Wavelength	121.6 nm
	Effective focal length	4100 mm
	Primary mirror	Parabolic
	Second mirror	Hyperbolic
	Detector pixel size	10 μm
	Focal plane size	45.8 mm × 45.8 mm
	Spatial resolution	1.0″
WST	Wavelength	360 nm
	Effective focal length	4100 mm
	Primary mirror	Parabolic
	Second mirror	Hyperbolic
	Detector pixel size	10 μm
	Focal plane size	45.8 mm × 45.8 mm
	Spatial resolution	1.0″

The optical designs of SDI and WST are optimized by geometrical ray tracing calculations with Zemax OpticStudio. The imaging performance of the design can be evaluated using the spot diagrams in Figure 10, the MTF in Figure 11 and the encircled energy curves in Figure 12. From the figures, the imaging performance is good for SDI and WST, and the spatial resolution can be less than 1.2″.

2.2 Mechanical Design

The mechanical structure of the LST adopts a whole design for saving space and reducing weight, and three instruments share a common supporting board. The structures include two parts: the LST instrument structure and the control electric box (CEB). The instrument structure is located outside the upper cabin, while the CEB is installed in the satellite cabin to facilitate power supply and thermal control. Because of the good operation environment, the design of the CEB mainly focuses on the sup-
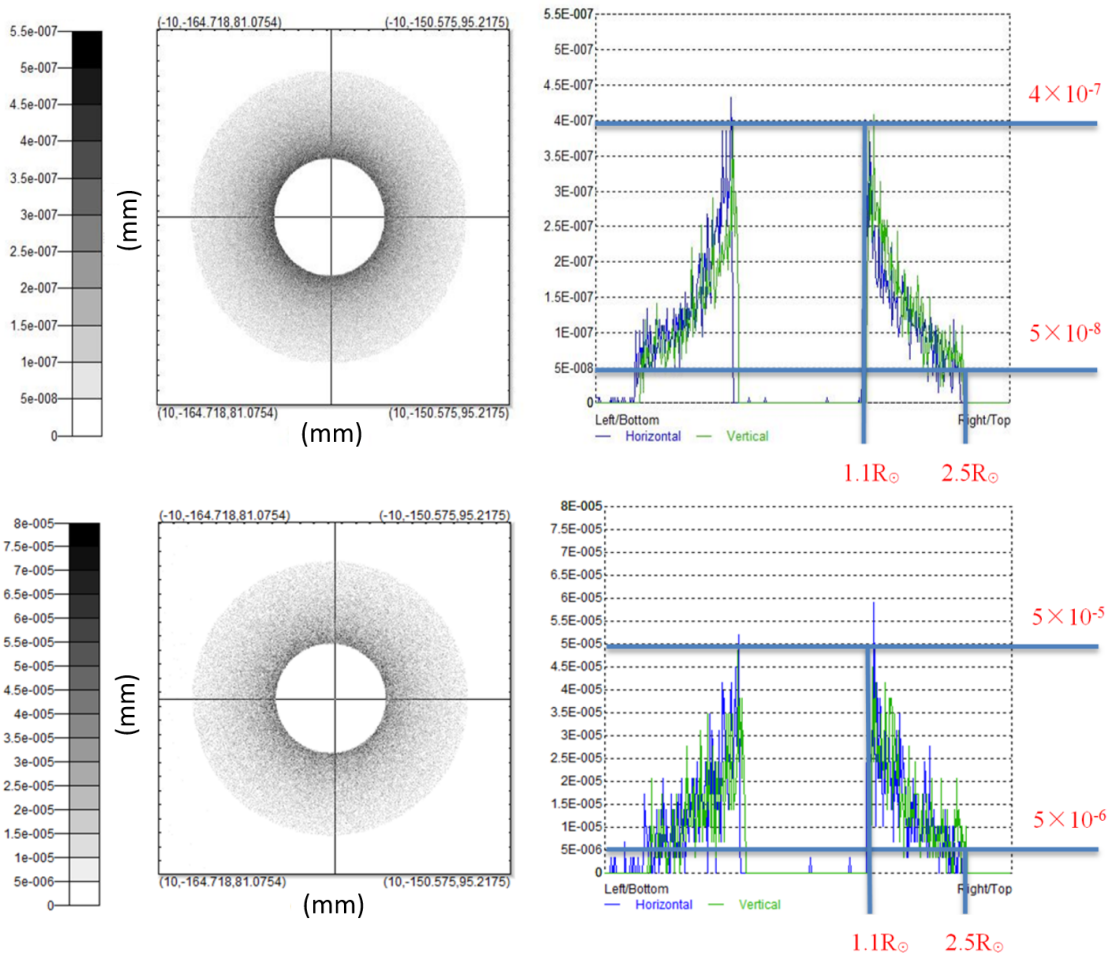
Fig. 9 Stray-light simulation results at 700 nm (*upper panels*) and 121.6 nm (*lower panels*).
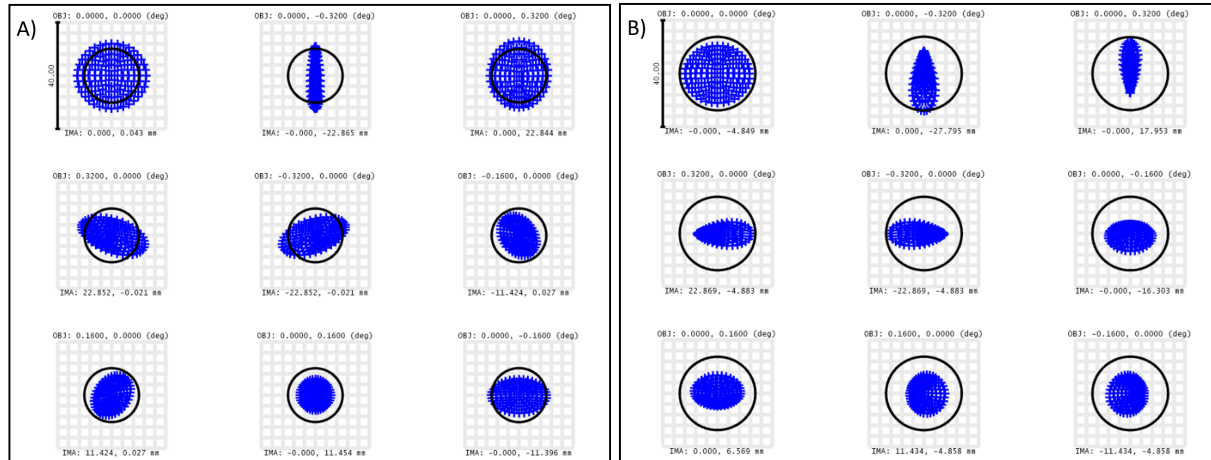

Fig. 10 Spot diagram of SDI (*left*) and WST (*right*).

port stiffness, anti-electromagnetic interference and anti-particle radiation. Meanwhile, the problems of heat dissipation and lightweight structure should be considered. The LST instrument structure includes several components: the SCI, SDI, WST, GT, an Imaging Box (IB), radiator, a suite of thermal control components and a main support structure. The main supporting structure holds all the LST instruments, associated harnesses, IC and thermal blankets.

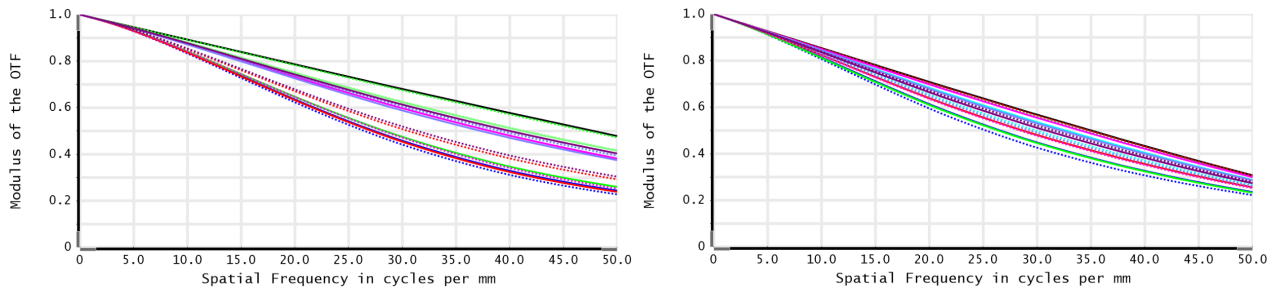Figure 14 illustrates the layout of the LST structure, which is divided into two parts, the top cabin and the bot-
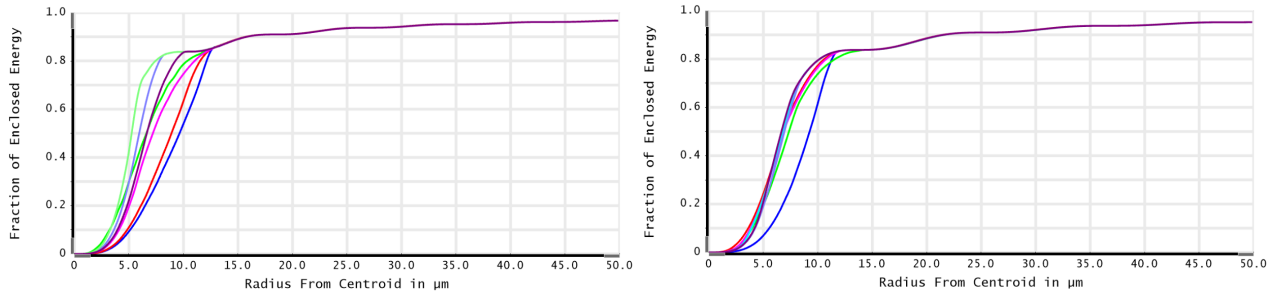
Fig. 11 MTF curves for SDI (*left*) and WST (*right*).

Fig. 12 Encircled energy distribution curves for SDI (*left*) and WST (*right*).
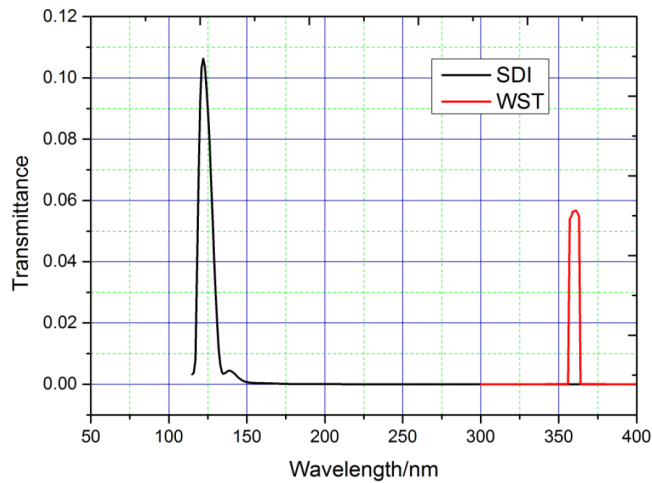

Fig. 13 Transmittance distribution of SDI and WST.

tom cabin. The top cabin contains the SCI optics, SCI imaging electronics and Imaging Control Box (ICB). The bottom cabin houses the SDI, WST, GT and SDI, and WST Imaging Electronics. The radiator is installed on the satellite platform surface to disperse heat from detectors, imaging electronics and solar radiation. SDI, WST, radiator and GT are described in more detail, which are traditional structure designs. Further description of SCI structure, main supporting structure and active mirror will be given below.

The SCI is composed of an active primary mirror (M1), secondary mirror (M2), third mirror (M3), beam splitter (M4), folding mirror (M5), light trap, door mechanism, light-reducing mechanism, 700 nm filter and polar-izer, Lyα filter wheel, two CMOS detectors and baffles. All of them are mounted on the main support structure. The surfaces of main support, and the baffles and cover are anodized and dyed a dense black to attenuate scattered light and meet the requirements of stray-light suppression. The SCI structure is shown in Figure 15.

2.2.1 Supporting structure

The main supporting structure provides an optical bench for the SCI optics sub-assemblies, SDI, WST, GT, electronics boxes and associated subsystems and thermal blankets. Considering the stringent mass budget as well as the mechanical and thermal requirements, SiC/Al materials are
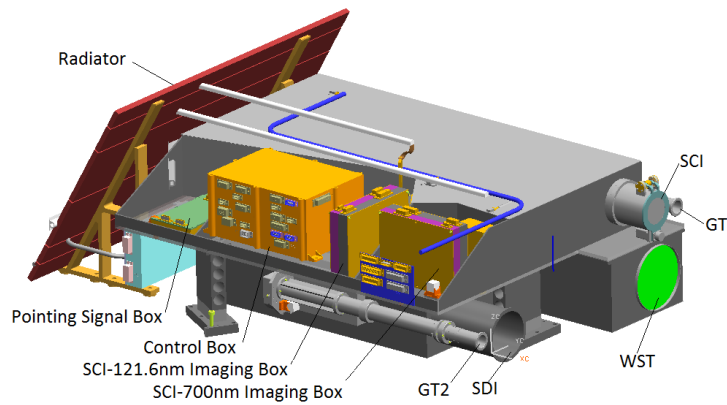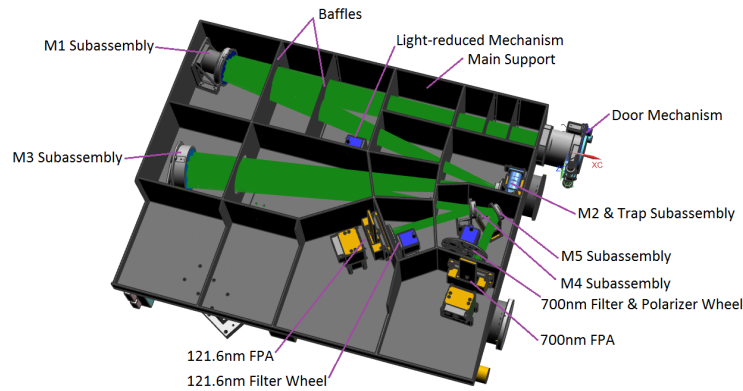
Fig. 14 Layout of the LST structure.

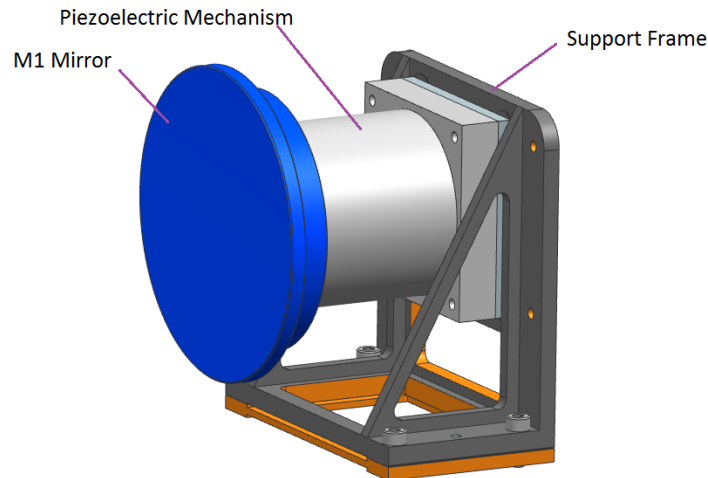**Fig. 15** Layout of SCI and the main support.

Fig. 16 M1 sub-assembly.

applied, which have a low coefficient of thermal expansion (CTE) and a higher stiffness, and are chosen to maintain a stable position between the mounting interfaces of the ASO-S satellite and LST. The SiC/Al composite is utilized widely by virtue of its higher stiffness-to-mass ratios and low outgassing properties. Lightweight holes appear in the form of triangles, quadrangles, hexagons and a few of special shapes. If they have the same rib length and thickness, the lightweight triangular structure has good stiffness compared with the others, but its lightweight efficiency is bad.

Meanwhile, the hexagonal structure has high efficiency because it is lightweight, but its stiffness is the least. Then, the quadrilateral is chosen to lighten the main structure weight for its moderate structural stiffness and lightweight efficiency, and convenience in mounting parts. The optimal structure of the main support is achieved through comparing simulation results and optimized lightweight design. The lightweight ratio of the optimized structure is around 80%.

A near-kinematic mounting scheme is also adopted. The kinematic mounting scheme includes three SiC/Al mounts with flexure for the main body of the telescope. It is realized by one mount located on the center line of the structure and the other two mounts symmetrically distributed about the center line. By adjusting the direction and position of the flexure mounts, the requirements of structural mechanics and stability can be achieved. The mounting scheme can minimize thermal stress in the telescope, guaranteeing mechanical and thermal stability of the telescope.

2.2.2 Active mirror

In the LST, there are two active mirrors for image stabilization, which are the SCI primary mirror and the SDI secondary mirror. The SCI M1 subassembly includes a mirror (M1, $\Phi93$ mm), a piezoelectric (PZT) mechanism and a support frame, as displayed in Figure 16.

The M1 mirror takes into account the objective mirror and image stabilization mirror driven by a piezoceramic actuator with a fast dynamic response of 100 Hz and a $0.12''$ angular resolution. The SCI M1 is chosen to bond the mirror and the invar support with epoxy resin to reduce the effect of mounting stress and thermal loads. The invar is chosen to support the mirror as its CTE is similar to that of fused silica. Matching the CTE of different structures can reduce the influence of temperature changes on the shape of the mirror surface.

2.3 Thermal design

2.3.1 Outer track heat flow

LST will operate in a 720 km Sun-synchronous orbit (SSO). The entrance port (+X direction) is oriented towards the Sun. The operating conditions of high temperature occur on the winter solstice, and the low temperature working conditions happen on the summer solstice. The average values of the external heat flow with respect to the high temperature and low temperature conditions are provided in Table 4. The −X surface has the smallest and stable external heat flow, which is suitable for being the heat dissipation surface of the detectors. The +Z plane and −Y

plane are suitable for being the electronic heat sinks from the perspective of external heat flow.

2.3.2 Thermal control index

The temperature range requirements for LST storage and operation in orbit are listed in Table 5. The mounting substrate and GT require an operating temperature of 19 to 25°C. All the four detectors need to work in a low temperature range of –45 to –20°C to keep the dark current at a low level. The electrical boxes operate in a temperature range between –30 and +45°C.

2.3.3 Internal thermal sources and main thermal design

Figure 17 depicts the schematic diagram of the LST heat sink. Heat generated by operation of the four CMOS detectors, SDI imaging electronics box and the WST imaging electronics box directly or indirectly flows to the −X heat sink. The heat power is radiated to the cold black space by heat sinks composed of aluminum alloy. The heat sink in the −X direction has a size of 790 mm (Y direction) by 525 mm and is divided into seven pieces. The heat sink stays at an angle of 30° with respect to the vertical direction.

2.3.4 Thermal analysis result

According to the aforementioned data analysis, the thermal control of LST is realized by a combination of active thermal control and passive heat dissipation. The analysis results are depicted in Figure 18, which have significant thermal improvement on the corresponding components, including 23 active thermal control heating zones and 44 main backup circuits. The thermistor temperature measurement circuit is 36 channels, and the PT1000 platinum resistance detector is eight channels, which finally achieves thermal control requirements. The analysis results demonstrate that the temperature of the visor is up to 91°C, but the visor is insulated from other parts. The thermal control material is also high temperature resistant material, which can meet the requirements of thermal control and operation during the expected lifetime. The lowest is the temperature of several detectors, which reaches −40°C. After thermal analysis in extreme conditions, the overall thermal design meets thermal control and expected lifetime requirements.
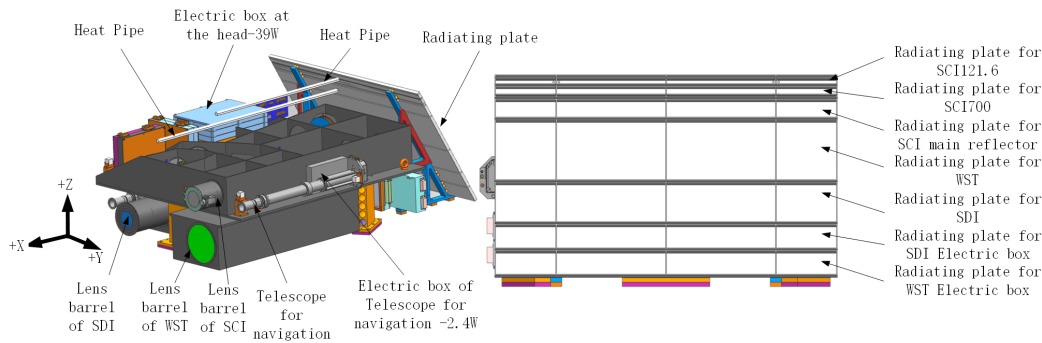
2.4 Electronic Design

LST electronics are composed of two main parts: the control electronics and imaging electronics as shown in Figure 19. The control electronics provide power supply, motor control, thermal control and housekeeping (Control

Table 4 Average Temperature of External Heat Flow at High Temperature and Low Temperature Conditions

Operation condition	The average of high temperature condition ($\mathrm{W\,m^{-2}}$)	The average of low temperature condition ($\mathrm{W\,m^{-2}}$)
+X	1477.4	1140.1
−X	60.5	78.0
+Y	84.5	91.8
−Y	84.5	92.4
+Z	96.3	71.3
−Z	73.2	104.7

Table 5 Thermal Control Index

Number	Part	Storage temperature (°C)	Operating temperature (°C)
1	Mounting substrate	0 — +30	+19 — +25
2	Telescope barrel for navigation	−10 — +30	+19 — +25
3	Electric box	−35 — +50	−30 — +45
4	Detectors	−50 — +30	−45 — −20
5	Motor	−10 — +30	+19 — +45
6	Filter	−10 — +30	+19 — +40
7	SCI primary mirror	−10 — +55	+19 — +55

Fig. 17 Internal heat source and main heat dissipation design.

Area Network, CAN) interface to the spacecraft. The control electronics box also contains a microprocessor, which receives and interprets uplinked commands, controls the image sequence, interfaces peripherals and performs housekeeping on data. The power supply converts the primary power of the ASO-S spacecraft to the required voltage values. The motor driving unit controls the seven stepper motors, which set positions of the filters and polarizers. The thermal control unit is responsible for maintaining the telescope in the operational temperature range. The control electronics have a backup design and the thermal control part has a cross backup design.

The imaging electronics contain four signal processing units and one image stabilization unit. The signal processing units are used to implement image acquisition and processing of data from the CMOS detectors, which read the image data at a rate of 280 Mbps via eight channels, and store the data in SDRAM. Then the data are transmitted to the spacecraft at a rate of 80 Mbps through Low Voltage Differential Signaling (LVDS) interfaces.

The image stabilization unit is composed of GT signal processing units and one PZT control unit, which is utilized to compensate spacecraft jitter in order to stabilize images on the detectors. The GT signal processing unit detects Sun-pointing errors, operating so that control software samples the GT signals every 0.25 ms and transmits them to the ASO-S spacecraft attitude control system (ACS) every 25 ms. In the LST, a redundant GT is designed for maintaining high reliability and one of the two GTs can be selected to be the pointing signal input of the ACS and the PZT control unit.

The flight software is responsible for receiving the command and orbital parameters from the spacecraft and transmits the science data to the spacecraft. It also handles the interfaces for the motors, heaters, GTs, PZTs and cameras. The software controls the imaging sequence of the camera to provide different operating modes, such as full-frame or windowed, auto-exposure control (AEC), decontamination, flare detection (FLD) and calibration. It is also responsible for the in-orbit adjustment of gains for CMOS sensors and image stabilization.
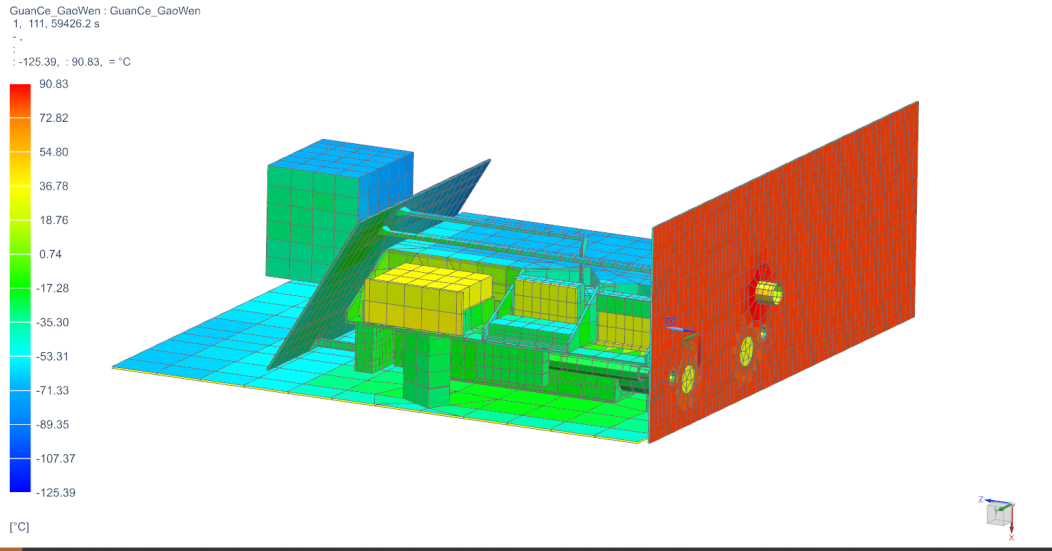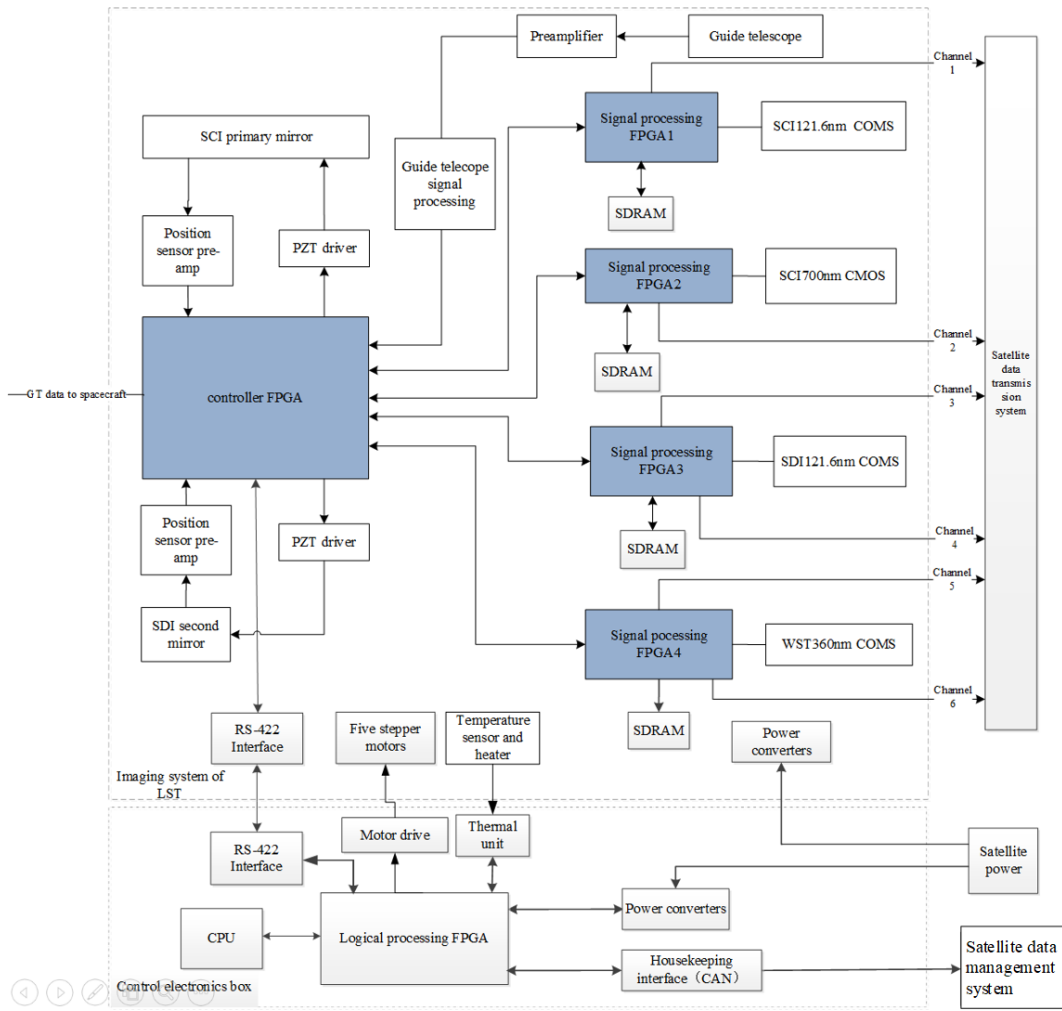
Fig. 18 Thermal analysis results of LST.

Fig. 19 Block diagram of LST electronics system.

3 TEST AND CALIBRATION

Based on the scientific objectives and technical requirements of LST, testing and calibration for various technical specifications should be performed. The testing items include working wavelength, angular resolution, FOV and stray-light suppression capability. The calibration items mainly include laboratory radiometric calibration and geometric calibration, in-flight radiometric and flat-field calibration (He et al. 2016). Testing items such as working wavelength, resolution, FOV and geometric calibration are basically the same as those of conventional imaging instruments. The stars with known irradiation are used for in-flight radiometric calibration, which is not described in this paper. The testing and calibration methods for stray-light suppression, laboratory radiometric calibration and in-flight flat-field calibration are different from those of conventional instruments, which are described in the following subsections.

3.1 Stray-light Measurement

Stray-light is one of the most important issues for SCI, since it images the weak corona near very strong solar disk light. Instead of employing a strong solar simulator, we implement high sensitivity stray-light testing technology to measure the stray-light, which applies a photon counting imaging detector (Wang et al. 2015) to measure the weak stray-light radiation generated by SCI. With the measured data, we can derive the stray-light of SCI so as to check whether the stray-light requirement is met.

The stray-light measurement device is composed of a solar radiation simulator and a photon counting imaging detector as diagrammed in Figure 20. An aperture and a diffuser are mounted on the focal plane of the collimator, along with the beam shaping lens and a high-brightness mercury xenon lamp to simulate solar radiation. The light outside the FOV of solar disk radiation is blocked by the aperture. Then, the high-intensity radiation generated by the light source passes through the collimator to form a divergence angle of $32'$, which illuminates SCI. The photon counting imaging detector is used to measure the stray-light brightness generated by the SCI and brightness of the simulated solar image. The ratio of the brightness of stray-light and the simulated solar disk represents the stray-light suppressing capability of SCI.

This stray-light measurement method avoids the necessity of a strong solar simulator with the brightness of one solar constant, in particular at 121.6 nm and 700.0 nm, and solves the problem of stray-light measurement at different wavelengths. It ensures that the SCI stray-light suppression capability satisfies the LST requirements.

3.2 Laboratory Radiometric Calibration

Radiometric responsivity is an important parameter describing the characteristics of LST, and radiance response is typically used to characterize the relationship between the output of an instrument and the radiation of a target. In the ultraviolet and visible wavelengths (VUV), an integrating sphere with known radiance at its exit aperture is generally employed to measure the radiometric response of an instrument, such as the WL wavelength of SCI and WST. Unfortunately for the Lyα waveband used by SCI and SDI, there is no integrating sphere available with known radiance, so we have designed an Lyα radiometric calibration device, which is composed of a VUV deuterium lamp, an Lyα filter, an MgF$_2$ diffuser, a small square target of known size, an FUV collimator and a high vacuum tank (Fig. 21).

The instrument to be calibrated and AXUV100G are mounted on the rotation table inside the high vacuum tank, while the target with known size is mounted on the focal plane of the collimator and illuminated by the VUV deuterium lamp through a 121.6 nm narrowband filter and an MgF$_2$ diffuser. When the vacuum satisfies the requirement that the VUV deuterium lamp works well, the collimator emits 121.6 nm parallel light. Firstly, the transfer standard detector of AXUV-100G is utilized to calibrate the brightness of the target with known size, and then rotates the table so that the instrument being calibrated can directly image the target. Comparing the radiance of the target with the gray scale of the output image, the radiometric response calibration data of the instrument can be obtained. The radiometric responsivity can be calculated according to Equation (4)

$$R = \frac{\text{Pixelvalue}}{S}. \tag{4}$$

Here R is brightness of the target, Pixelvalue is gray scale of the image and S is radiometric responsivity of the instrument. Both the SCI Lyα channel and SDI employ the above method for laboratory radiometric calibration. The estimated error is 5%, which depends on how errors are transferred from the standard detector, rotation error of the table and stability of the solar simulator.

3.3 In-flight Flat-field Calibration

Due to non-uniformity in the detector response and vignetting of the optics, the response at different positions of the focal plane is not uniform. Flat-field calibration is applied to correct non-uniformity of the response and to eliminate the effects of non-uniformity in the response on imaging. Meanwhile, as the in-flight time increases, the radiometric responsivity may change. Therefore, it is neces-
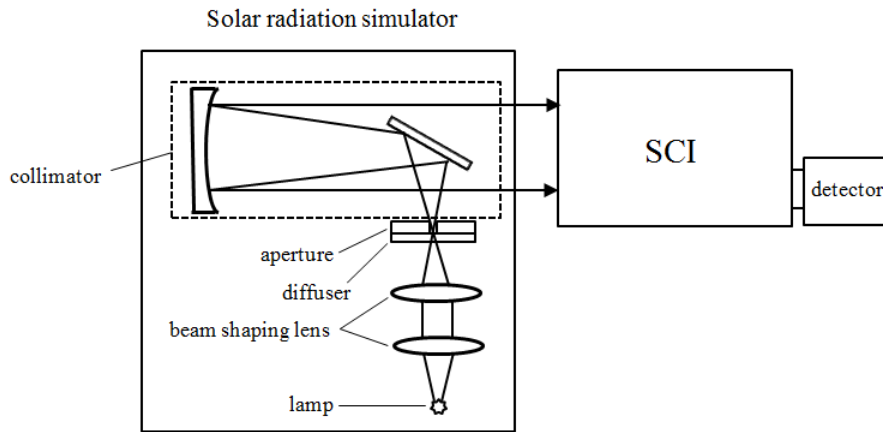
Solar radiation simulator

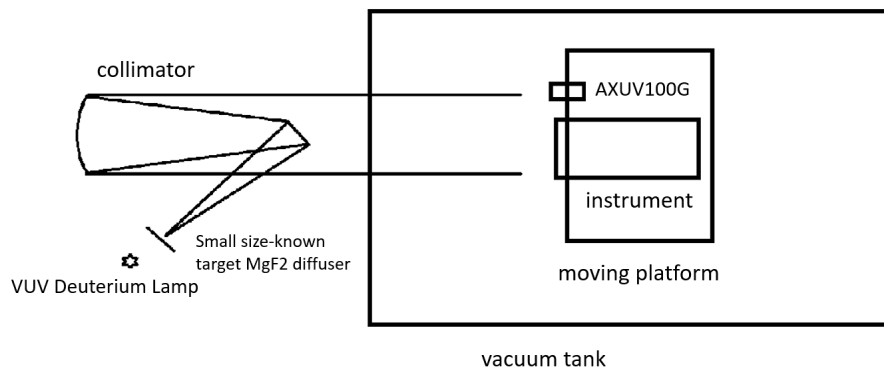**Fig. 20** Schematic diagram of the stray-light measurement device.

Fig. 21 Schematic diagram of radiometric response calibration at 121.6 nm.

sary to regularly obtain the flat field so as to get more accurate solar disk and coronal images. Different flat-field calibration methods are used for different channels and wavelengths to satisfy the requirements of in-flight calibration.

SCI is composed of two coronal imaging channels, i.e., the Lyα and 700.0 nm wavebands. The two channels share common optics. In order to achieve in-flight flat-field calibration for SCI, a transmissive diffuser is mounted in the middle of the primary mirror and the secondary mirror, and is imaged by the secondary mirror and subsequent optics. Since the transmissive diffuser is far from the focal plane of the primary mirror, the beam is defocused, and uniformity of the beam is largely the same as that of the entrance aperture. Therefore, the transmissive diffuser is mostly illuminated by uniform light, and a uniformly diffused image is formed in the focal plane of the imaging channel. Meanwhile, the scattering distribution and non-uniformity of the diffuser can be calibrated in the laboratory using the integrating sphere. In addition, the laboratory calibration data can be stored and the in-flight flat-field calibration result can be corrected to obtain highly accurate flat-field calibration data. The accuracy of the flat-field calibration using this method is expected to be 2%, which mainly de-

pends on the distribution of the scattering characteristics of the transmissive diffuser, the accuracy of the flat-field calibration on the ground and the positional accuracy of the diffuser.

The Sun is a perfect source for in-flight flat-field calibration for SDI and WST. In the field of space-based solar imaging, the Kuhn-Lin-Loranz (KLL) flat-field calibration method (Kuhn et al. 1991) is often employed for in-flight flat-field calibration, which can avoid necessitating uniform illumination. This method has been applied in many solar observation platforms such as SOHO and SDO, and is a mature and reliable in-flight flat-field calibration scheme with high accuracy. Therefore, both SDI and WST will use the KLL method to achieve in-flight flat-field calibration data.

4 SUMMARY

LST, as one of the three payloads onboard the ASO-S mission, is composed of three instruments and four imaging channels. The integrated design scheme is implemented to save space and reduce weight on the premise of ensuring structural stability and structural stiffness. The de-

signing results are estimated to have an envelope size of $1280 \times 790 \times 475\,\text{mm}^3$ with a weight of $93\,\text{kg}$ and power consumption of $158\,\text{W}$.

Among the three telescopes of LST, SCI is a Lyot-type dual-waveband internally occulted reflecting and off-axis coronagraph with high spatial resolution and smaller vignetting. The light trap is designed behind the secondary mirror to absorb solar disk radiation. The beam splitter is arranged in front of the focal plane assembly to separate $121.6\,\text{nm}$ and $700.0\,\text{nm}$ radiation for simultaneous imaging in both the Lyα line and WL waveband. In addition, the beam splitter has the function of narrowband filtering to suppress out-of-band radiation and achieve high-spectral purity imaging in the Lyα line.

SDI and WST are devoted to observations of the solar disk with the off-axis two-mirror reflective layout to reduce the number of optical components and improve the energy transfer efficiency. The narrowband multilayer mirrors and corresponding filters are utilized to prevent unwanted radiation from reaching the detector. When working in orbit, the effect of out-of-band radiation associated with $121.6\,\text{nm}$ and $360\,\text{nm}$ imaging can be effectively suppressed.

LST has the characteristics of compact structure, lightweight, good optical performance and high reliability. It is suitable for space applications and meets the scientific objective requirements.

References

Antonucci, E., Romoli, M., Andretta, V., et al. 2019, A&A, in press

Brueckner, G. E., Howard, R. A., Koomen, M. J., et al. 1995, Sol. Phys., 162, 357

Chen, B., & He, F. 2011, Optics and Precision Engineering, 19, 2057 (in Chinese)

Chen, B., Song, K.-F., Li, Z.-H., et al. 2014, RAA (Research in Astronomy and Astrophysics), 14, 1654

Feng, L., Li, H., Chen, B., et al. 2019a, RAA (Research in Astronomy and Astrophysics), 19, 162

Feng, L., Li, H., Inhester, B., et al. 2019b, RAA (Research in Astronomy and Astrophysics), 19, 059

Fineschi, S., Antonucci, E., Naletto, G., et al. 2012, in Society of Photo-Optical Instrumentation Engineers (SPIE) Conference Series, Vol. 8443, Proc. SPIE, 84433H

Gan, W., Zhu, C., Deng, Y., et al. 2019, RAA (Research in Astronomy and Astrophysics), 19, 156

He, L., Chen, B., Zhong, H., Liu, S., & Wang, X. 2016, Optics and Precision Engineering, 24, 1036 (in Chinese)

Kuhn, J. R., Lin, H., & Loranz, D. 1991, PASP, 103, 1097

Landini, F., Vives, S., Romoli, M., et al. 2017, in Society of Photo-Optical Instrumentation Engineers (SPIE) Conference Series, 10564, Proc. SPIE, 105640F

Li, H., Chen, B., Feng, L., et al. 2019, RAA (Research in Astronomy and Astrophysics), 19, 158

Li, Y., Zhang, H., Wang, H., et al. 2014, Applied Surface Science, 317, 902

Sandri, P., Fineschi, S., Romoli, M., et al. 2018, Optical Engineering, 57, 015108

Vial, J.-C., Auchère, F., Chang, J., et al. 2007, Advances in Space Research, 40, 1787

Wang, X., Chen, B., & Yao, L. 2018, Applied Spectroscopy, 72, 943

Wang, X.-D., Chen, B., Wang, H.-F., et al. 2015, Scientific Reports, 5, 8503

Zhang, X.-X., Chen, B., He, F., et al. 2019, Light: Science & Applications, 8, 47